RADIATION PROBLEMS AT LINEAR e^+–e^- COLLIDERS

R.Engel
Institut für Theoretische Physik, Universität Leipzig,
D–04109 Leipzig Germany
and Fachbereich Physik, Universität Siegen, D–57068
Siegen, Germany
A.Ferrari, P.R.Sala
INFN, Sezione di Milano, Via Celoria 16, I–20133
Milano, Italy
and
J.Ranft
Laboratoire de Physique Théorique LAPP
Groupe d'Annecy: LAPP, Ch. de Bellevue, BP 110,
F-74941 Annecy-le-Vieux Cedex, France.

Abstract

Hadronic photon-photon collisions are investigated in the framework of the two-component Dual Parton Model. The model contains contributions from direct, resolved soft and resolved hard interactions. All free parameters of the model are determined in fits to hadron-hadron and photon-hadron cross section data.

The model is then applied to the calculations of the radiation environment for detectors at future e^+–e^- colliders. The results of these studies are compared with similar studies carried out for the ATLAS detector at LHC. While integrated radiation levels due to hadronic photon-photon collisions are shown to be many orders of magnitude lower than at LHC, instantaneous values are demonstrated to be a source of major concern. For this last topic, significant differences can be anticipated between superconducting (TESLA) and room temperature (NLC/SBLC) projects due to the different time structure of the beam, with expected peak levels for the latter ones not so far from LHC ones.

1 INTRODUCTION

The photon, in its high-energy interactions with hadrons, behaves very much like a hadron, however with cross sections reduced strongly against pure hadronic cross sections. Besides this hadronic interaction, usually described using the Vector Dominance Model, the photon has a direct pointlike interaction with hadronic constituents. At moderate energies the hard interactions of the photons do not change significantly the general picture of photon-hadron and photon-photon interactions. Even at high energies, hadronic interactions of photons are characterized by soft multiparticle production. Since the soft component of hadron production cannot be understood purely on the basis of perturbative QCD one has to rely on models like the Dual Parton Model [1] or the model by Schuler and Sjöstrand [2, 3] to calculate multiparticle final states. Assuming an universal behavior of soft hadronic interactions, the Dual Parton Model (DPM) can be extended to hadronic interactions involving photons [4, 5]. Here we apply the model described in [4, 5, 6] to the study of hadronic photon-photon interactions.

The model is used to calculate the radiation problems in a typical collider detector due to the hadrons produced in photon–photon collisions in the interaction region of a linear e^+–e^- collider. It must be stressed that only *hadronic* photon–photon collisions are discussed in this work, and that a significant contribution to the total radiation environment will come from processes like $\gamma\gamma \to e^+e^-$ and $\gamma\gamma \to \mu^+\mu^-$, whose cross sections are significantly larger than for $\gamma\gamma \to hadrons$. However the latter processes are expected to produce most of the hadrons, which are the dominant source of damage for semiconductor based devices and usually the main contribution to particle punchthrough from the detector.

The calculated radiation levels are discussed both in terms of integrated levels, which are of interest for damage, ageing and radioactivation of detector components, and in terms of instantaneous rates of particles in the detector itself, which are of maximum importance for the safe operation of the apparatus, due to their impact on pattern recognition, detector occupancy and above all trigger rate and efficiency. While the former effects are fairly insensitive to the specific collider design under consideration, depending only on energy and luminosity, the latter ones are indeed strongly dependent on the beam time structure. Therefore, TESLA and NLC has been used as representatives of two very different beam time structures, and the difference between them has been investigated and shown to be significant for instantaneous rates, NLC being on the bad side.

2 THE EVENT GENERATOR PHOJET

The realization of the DPM with a hard and a soft component in PHOJET is similar to the event generator DTUJET-93 [7, 8]. In the model, the dual nature of the photon is taken into account by considering the physical photon state as a superposition of a "bare photon" and virtual hadronic states having the same quantum numbers as the photon. Two generic hadronic states

$|q\bar{q}\rangle$ and $|q\bar{q}^\star\rangle$ have been introduced to describe the hadronic piece of the photon. The low-mass state $|q\bar{q}\rangle$ corresponds to the superposition of the vector mesons ρ, ω and ϕ and a $\pi^+\pi^-$ background. The state $|q\bar{q}^\star\rangle$ is used as an approximation for hadronic states with higher masses. The physical photon reads

$$|\gamma\rangle = \sqrt{Z_3}\ |\gamma_{\rm bare}\rangle + |\gamma_{\rm had}\rangle \tag{1}$$

with

$$Z_3 = 1 - \frac{e^2}{f^2_{q\bar{q}}} - \frac{e^2}{f^2_{q\bar{q}^\star}} \tag{2}$$

and

$$|\gamma_{\rm had}\rangle = \frac{e}{f_{q\bar{q}}}\ |q\bar{q}\rangle + \frac{e}{f_{q\bar{q}^\star}}\ |q\bar{q}^\star\rangle \tag{3}$$

where e denotes the elementary charge.

The interactions of the hadronic fluctuations are described within the Dual Parton Model in terms of reggeon and pomeron exchanges. For soft processes, photon-hadron duality is used. The energy-dependence of the reggeon and pomeron amplitudes is assumed to be the same for all hadronic processes. Therefore, data on hadron-hadron and photon-hadron cross sections can be used to determine the parameters necessary to describe soft photon-photon interactions. The pomeron exchange is subdivided into processes involving only *soft* processes and all the other processes with at least one large momentum transfer (*hard* processes) by applying a transverse momentum cutoff $p_\perp^{\rm cutoff}$ to the partons. On Born-graph level, for example, the photon-photon cross sections is built up by: **(i)** reggeon and pomeron exchange (soft processes only), **(ii)** hard resolved photon-photon interaction, **(iii)** single direct interactions, and **(iv)** double direct interactions. If not explicitly stated, all the Parton Model calculations of the hard processes have been done using the leading order GRV parton distribution functions for the proton [9] and the photon [10].

The amplitudes corresponding to the one-pomeron exchange between the hadronic fluctuations are unitarized applying a two-channel eikonal formalism similar to [7]. In impact parameter representation, the eikonalized scattering amplitude for resolved photon interactions has the structure

$$a_{\rm res}(s,B) = \frac{i}{2}\left(\frac{e^2}{f^2_{q\bar{q}}}\right)^2\ \left(1 - e^{-\chi(s,B)}\right) \tag{4}$$

with the eikonal function

$$\chi(s,B) = \chi_S(s,B) + \chi_H(s,B) + \chi_D(s,B) + \chi_C(s,B). \tag{5}$$

Here, $\chi_i(s,B)$ denotes the contributions from the different Born graphs: (S) soft part of the pomeron and reggeon, (H) hard part of the pomeron (D) triple- and loop-pomeron, (C) double-pomeron graphs.

The probabilities to find a photon in one of the generic hadronic states, the coupling constants to the reggeon and pomeron, and the effective reggeon and pomeron intercepts cannot be determined by basic principles. These quantities are treated as free parameters and determined by cross section fits [4]. In Fig. 1 we show the model predictions for the inelastic photon-photon cross section (including quasi-elastic vector meson production).

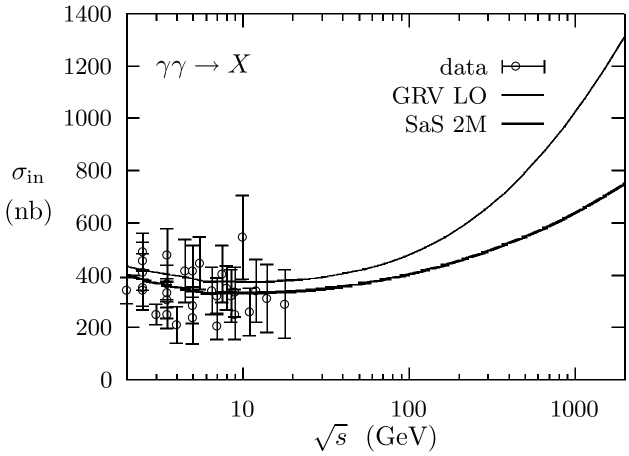

Figure 1: *Inelastic photon-photon cross section calculated with the model and compared with data [4]. The two curves from the model were calculated using the GRV LO photon structure function [10] and the SaS 2M photon structure function [11].*

The probabilities for the different final state configurations are calculated from the discontinuity of the scattering amplitude (optical theorem) which can be expressed as a sum of graphs with k_c soft pomeron cuts, l_c hard pomeron cuts, m_c triple- or loop-pomeron cuts, and n_c double-pomeron cuts by applying the Abramovski-Gribov-Kancheli cutting rules [12, 13]. In impact parameter space one gets for the inelastic cross sections

$$\sigma(k_c, l_c, m_c, n_c, s, B) =$$

$$\frac{(2\chi_S)^{k_c}}{k_c!}\frac{(2\chi_H)^{l_c}}{l_c!}\frac{(2\chi_D)^{m_c}}{m_c!}\frac{(2\chi_C)^{n_c}}{n_c!}\exp[-2\chi(s,B)]. \tag{6}$$

Since the triple-, loop-, and double-pomeron graphs are objects involving several pomerons, a further resummation is done [7, 6] to allow for the probability interpretation of Eq. (6).

For pomeron cuts involving a hard scattering, the complete parton kinematics and flavors/colors are sampled according to the Parton Model using a method similar to [14], extended to direct processes. For pomeron cuts without hard large momentum transfer, the partonic interpretation of the Dual Parton Model is used: photons or mesons are split into a quark-antiquark pair whereas baryons are approximated by a quark-diquark pair. The longitudinal momentum fractions of the soft partons are given by Regge asymptotics [15, 16]. The transverse momenta of the soft partons are sampled from an exponential distribution in order to get a smooth transition between the transverse momentum distributions of the soft constituents and the hard scattered partons. In diffraction dissociation or double-pomeron scattering, the parton configurations are generated using the same ideas described above applied to pomeron- photon/pomeron scattering processes. Finally, the fragmentation of the sampled partonic final states is done by forming color neutral strings between the partons according to the color flow. In the limit of many colors in QCD, this leads to the two-chain configuration characterizing a cut pomeron and a one-chain system for a cut reggeon. The chains are fragmented using the Lund fragmentation code JETSET 7.3 [17].

In [5]. we present a few comparisons of PHOJET results with hadron-hadron and photon-hadron data in order to illustrate, that the model as formulated in PHOJET is very well able to describe these channels. For photon-photon collisions we have to rely on the predictive power of the model.

3 COMPARISON OF MINIMUM-BIAS HADRON PRODUCTION IN HADRON–HADRON, PHOTON–HADRON AND PHOTON–PHOTON COLLISIONS

In this Section we compare the model predictions for inelastic hadron production in proton-proton, photon-proton and photon-photon collisions at fixed center-of-mass (CMS) energies $\sqrt{s}$. Since elastic hadron-hadron collisions usually are excluded studying inclusive secondary distributions, we also exclude in the reactions with photons and photons the corresponding quasi-elastic diffractive channel i.e. $\gamma + \gamma/p \rightarrow V + V/p$, $(V = \rho, \omega, \phi)$.

In Figs. 2 and 3 we show the transverse momentum distribution at 20 and 200 GeV. and the transverse energy flow of proton-proton, photon-proton and photon-photon interactions at $\sqrt{s} = 200$ GeV.

The differences in the $p_\perp$ distributions come from the direct photon interaction and the fact, that the photon structure function is considerably harder than the proton structure function. However, these differences in the hard scattering do not strongly influence such properties of the collision as average multiplicities or the transverse energy flow. Minimum bias hadron production in hadron-hadron, photon-hadron and photon-photon collisions of the same CMS energy is remarkably similar. The only striking differences appear in the transverse momentum distribution or distributions, where the transverse momentum behavior is essential.

However, these differences in the hard scattering do not strongly influence such average properties of the collision as average multiplicities or even average transverse momenta. The total and charged multiplicities at all energies are rather near to each other in all channels. Also the average transverse momenta rise as expected from *p*-*p* over γ-*p* to γ-γ.

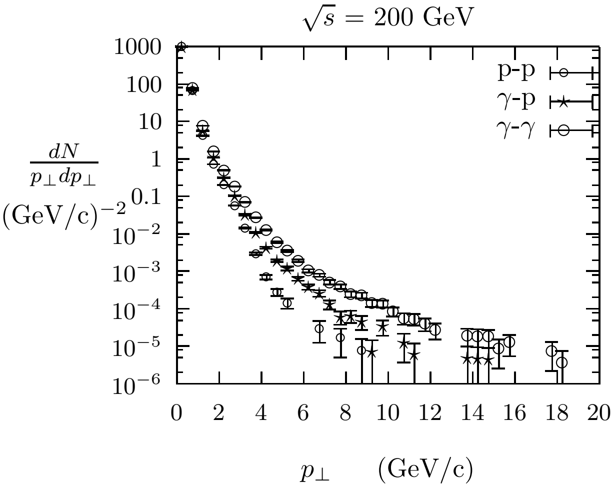

Figure 2: *Transverse momentum distributions of charged particles calculated with* PHOJET *for proton-proton, photon-proton and photon-photon interactions.*

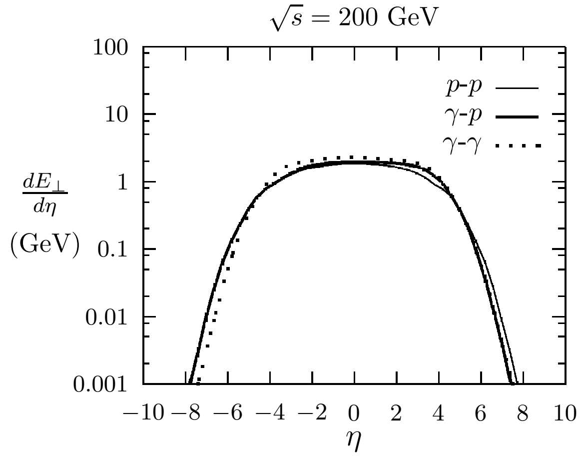

Figure 3: *Transverse energy flow calculated with* PHOJET *for proton-proton, photon-proton and photon-photon interactions.*

In Fig. 3 the transverse energy flow of proton-proton, photon-proton and photon-photon interactions at $\sqrt{s} = 200$ GeV on a logarithmic scale. In Fig. 4 we plot linearly the transverse energy distribution $dE_\perp/d\eta$. Roughly, these distributions should be equivalent to the pseudorapidity distribution $dN/d\eta$ multiplied with the average transverse energy per particle. We observe characteristic differences, which can be understood from the features already discussed. The transverse energy distribution is wider in photon-photon collisions than in proton-proton collisions. The transverse energy distribution rises at all η from *p*-*p* over γ-*p* to γ-γ. For γ-*p* the distribution agrees backwards with *p*-*p* and forwards with γ-γ.

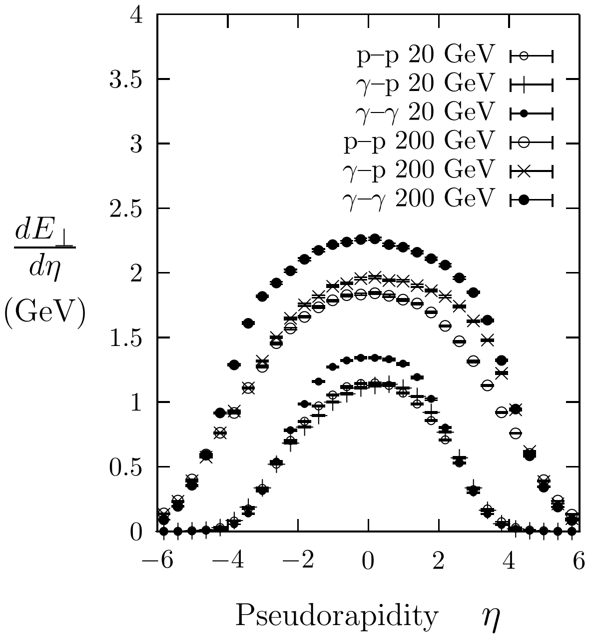

Figure 4: We compare at the collision energies $\sqrt{s} =$ 20 GeV and 200 GeV in a linear plot the distribution of the transverse energy $E_\perp$ as function of the pseudorapidity η for p-p, γ-p and γ–γ collisions. The calculation was done with PHOJET for inelastic collisions.

For *p-p* or *p̄-p* collisions the transverse energy distribution at $\eta = 0$ is known from ISR experiments and experiments at the CERN collider. The values calculated with PHOJET agree well with these measurements. At HERA it was found, that practically the same transverse energy at $\eta = 0$ is found like in *p-p* interactions and in collisions of real or virtual photons with protons. This observation agrees well with our results in Figs. 4 and 3.

The PHOJET model can be used to calculate hadronic events in hadron-hadron, photon-hadron and photon-photon collisions. The model is found to agree well with data in hadron-hadron and photon-hadron collisions, the predictions for photon-photon collisions do not need any new parameters.

4 HADRON PRODUCTION IN PHOTON-PHOTON COLLISIONS AT PRESENT AND FUTURE ELECTRON-POSITRON COLLIDERS

4.1 Photon flux calculation

Bremsstrahlung The flux of quasi-real photons is calculated using the equivalent photon approximation (improved Weizsäcker-Williams spectrum [18, 19, 20]). Within this approximation the $ep \to eX$ photoproduction cross section is given by

$$\frac{d\sigma_{ep}}{dy} = f_{\gamma,e}(y)\ \sigma_{\gamma p}(s,0) \tag{7}$$

with

$$f_{\gamma,e}(y) = \frac{\alpha_{\rm em}}{2\pi}\left[\frac{1+(1-y)^2}{y}\ln\frac{P^2_{\rm max}}{P^2_{\rm min}} - 2m_e^2 y\left(\frac{1}{P^2_{\rm min}} - \frac{1}{P^2_{\rm max}}\right)\right]. \tag{8}$$

Here, y and $P^2 = -p^2_\gamma$ denote the energy fraction taken by the photon from the electron and the photon virtuality. $\alpha_{\rm em}$ is the fine structure constant. Taking the kinematic limit $P^2_{\rm min,kin}$ as lowest photon virtuality allowed one gets with the electron mass m_e and

$$P^2_{\rm min,kin} = \frac{m_e^2 y^2}{1-y} \tag{9}$$

the spectrum of quasi-real photons

$$f_{\gamma,e}(y) = \frac{\alpha_{\rm em}}{2\pi}\left(\frac{1+(1-y)^2}{y}\ln\frac{(1-y)P^2_{\rm max}}{m_e^2 y^2} - \frac{2(1-y)}{y}\right). \tag{10}$$

A similar expression holds for $ee \to ee{+}X$ scattering involving quasi-real photons only

$$\frac{d^2\sigma_{ep}}{dy_1 dy_2} = f_{\gamma,e}(y_1)\ f_{\gamma,e}(y_2)\ \sigma_{\gamma\gamma}(s,0). \tag{11}$$

Beamstrahlung In case of Gaussian beams, the effective beamstrahlung spectrum has been estimated by Chen et.al. [21]. The dependence of this spectrum on the particle-bunch parameters can be expressed by the beamstrahlung parameter Y:

$$Y = \frac{5r_e^2 E N_e}{6\alpha_{\rm em}\sigma_z(\sigma_x+\sigma_y)m_e}. \tag{12}$$

Here, E denotes the beam energy, N_e is the number of electrons or positrons in a bunch, σ_x and σ_y are the transverse bunch dimensions, and $r_e = 2.818 \cdot 10^{-12}$mm is the classical electron radius. The beamstrahlung spectrum is approximated by [21, 22]

$$\begin{aligned} f^{\rm beam}_{\gamma,e}(y) &= \frac{\kappa^{1/3}}{\Gamma(1/3)}y^{-2/3}\left(1-y)\right)^{-1/3}e^{-\kappa y/(1-y)} \\ &\cdot \left\{\frac{1-w}{\tilde g(y)}\left[1-\frac{1}{\tilde g(y)N_\gamma}\left(1-e^{-N_\gamma \tilde g(y)}\right)\right]\right. \\ &+ \left. w\left[1-\frac{1}{N_\gamma}\left(1-e^{-N_\gamma}\right)\right]\right\}, \end{aligned} \tag{13}$$

with

$$\tilde g(y) = 1 - \frac{1}{2}(1-y)^{2/3}\left[1-y+(1+y)\sqrt{1+Y^{2/3}}\right] \tag{14}$$

and $\kappa = 2/(3Y)$, $w = 1/(6\sqrt{\kappa})$. The average number of photons N_γ emitted per electron is given by

$$N_\gamma = \frac{5\alpha^2_{\rm em}\sigma_z m_e}{2r_e E}\frac{Y}{\sqrt{1+Y^{2/3}}}. \tag{15}$$

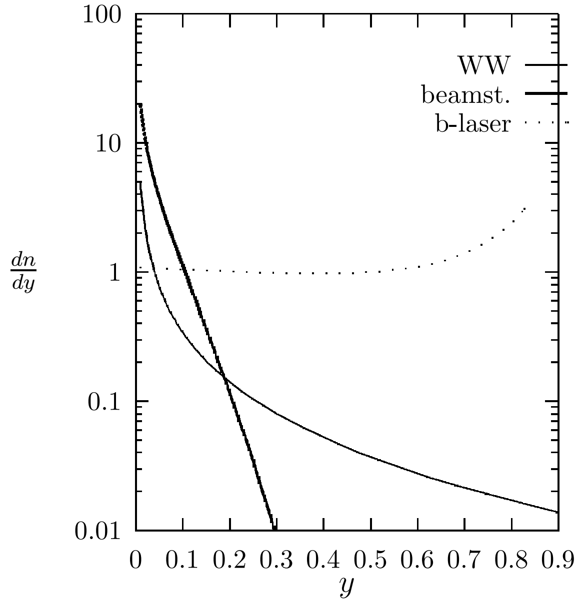

Figure 5: Photon fluxes at a $\sqrt{s} = 500$ GeV linear collider TESLA [26]. Given are the improved Weizsäcker-Williams spectrum, the beamstrahlung spectrum using the bunch parameters $N_e = 1.8\ 10^{10}$, $\sigma_x = 598$ nm, $\sigma_y = 6.5$ nm and $\sigma_z = 0.5$ mm [26], and a backscattered laser spectrum.

Photonemission by laser-backscattering Depending on the polarization of the laser light, various photon spectra can be produced [23, 24, 25]. Here we consider only the case of unpolarized laser radiation. Furthermore, we assume that the laser frequency is chosen to be below the pair-creation threshold at the optimal point. Then, the spectrum of backscattered photons can be written as [22]

$$f^{\mathrm{laser}}_{\gamma,e}(y) = \frac{-0.544\, y^3 + 2.17\, y^2 - 2.63\, y + 1.09}{(1-y)^2}\ \Theta(0.828 - y). \tag{16}$$

4.2 Hadrons produced in photon-photon collisions at e^+–e^- linear colliders

There are at present several projects for electron-positron linear colliders under active study. Here we pick out for our calculations only one of these projects, the TESLA linear collider. Details about the most recent TESLA project were given by Brinkmann [26].

Using the formulae discussed in the last subsection we plot in Fig. 5 the photon spectra according to the equivalent photon approximation, the beamstrahlung spectrum using the bunch parameters [26] as given in the caption of Fig. 5 and a backscattered laser spectrum. The photon virtuality was restricted to $P^2 \leq 0.01$ GeV^2/c^2. In Table 1 we give the average photon-photon energies and the weight factors in μb for the three photon spectra and two energies. From Fig. 5 and Table 1 we see, that the beamstrahlung spectrum of the TESLA project is the softest of the three photon spectra, the backscattered laser spectrum is the hardest. The parameters for the equivalent photon spectrum at the LEP-II energy, as well as those connected with the LHC p-p collider are also reported in Table 1 for comparison, since these two examples will be used in the next section when discussing the radiation environment for the detectors at future $e^+ - e^-$ colliders.

Table 1 Average photon–photon energies and weight factors in μb for the three photon spectra and two linear collider energies. Data for LEP–II and LHC are also reported for comparison.

$\sqrt{s}$	Photon spectrum	$\sqrt{s}_{\gamma\gamma}$	Weight (μb)
175	W.–W.	25	0.0032
500	W.–W.	50	0.0067
500	Beamst.	16.7	0.038
500	B.Laser	252	0.47
1000	W.–W.	105	0.0075
1000	Beamst.	41	0.026
1000	B.Laser	509	0.59
$\sqrt{s}$	Hadron spectrum	$\sqrt{s}_{pp}$	σ (μb)
14000	p-p	14000	80000

Of course, in the case of a linear collider we will always have to consider for background problems the superposition of the beamstrahlung spectrum and the equivalent photon spectrum.

A reasonable lowest energy for collisions to be sampled using PHOJET is $\sqrt{s}_{\gamma\gamma} = 5$ GeV (PHOJET would however run without problems even down to $\sqrt{s}_{\gamma\gamma} =$ 2 GeV). Therefore, for all applications in this and the following sections we always cut the photon spectra at small y in such a way, that this lower energy cut-off is respected.

5 RADIATION CALCULATIONS FOR A REALISTIC DETECTOR GEOMETRY

The photon-photon hadronic interactions as simulated by Phojet have been used to investigate the resulting radiation levels in a hypothetical detector for a future e$^+$-e$^-$ collider. The results for the various options/processes have been compared among themselves and with similar calculations carried out for one of the LHC detectors (ATLAS).

It is important to stress again that all numbers re-

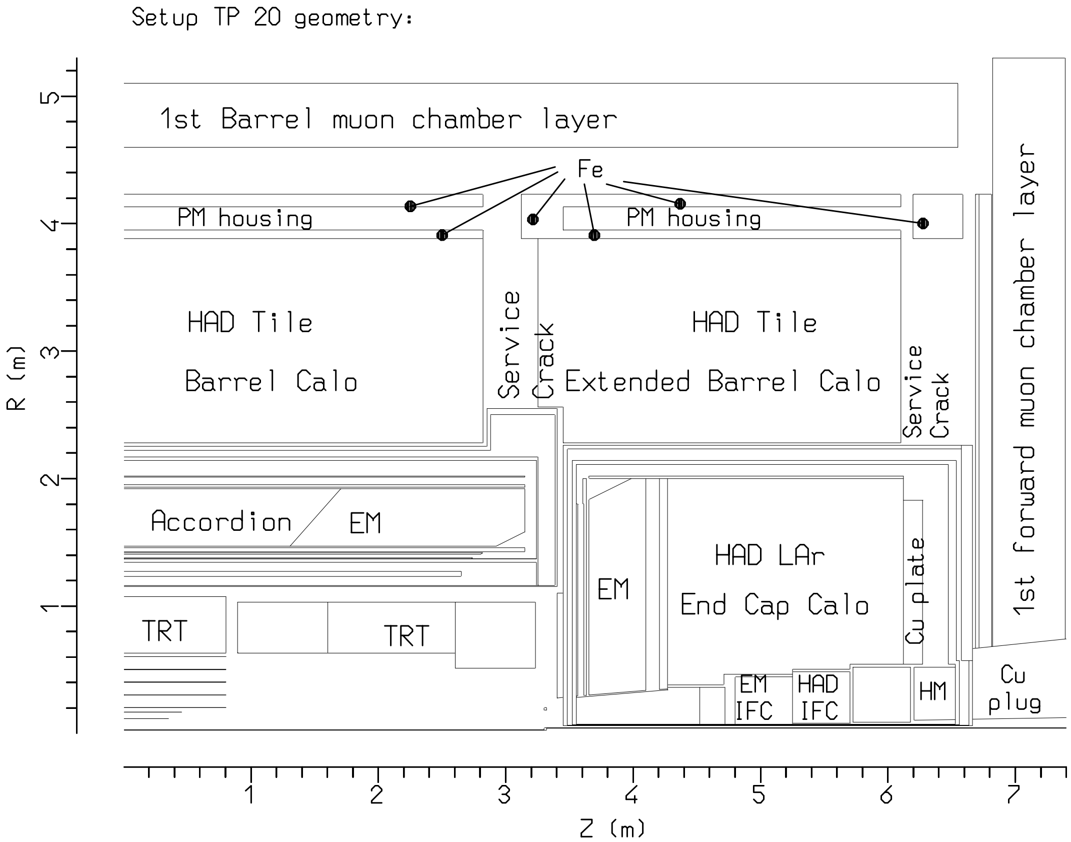

Figure 6: Schematic drawing of the geometry of the ATLAS detector used for all radiation calculations presented in this paper

ported in this work refer to the $\gamma\gamma \rightarrow$ *hadrons* processes only, which are believed to give the major contribution to hadron fluences in the detectors. Processes like $\gamma\gamma \rightarrow e^+e^-$ and $\gamma\gamma \rightarrow \mu^+\mu^-$ are not considered in this work, and their effect should be added to get the overall radiation environment.

5.1 Simulated Geometry

The geometry used for all calculations is the one adopted for the ATLAS calculations and it is shown in Fig. 6. Such a detector consists of a calorimeter system (barrel, End Cap and Forward Calorimeters) covering the pseudorapidity range $|\eta| \leq 4.8$. A 2 T solenoidal field is present in the detector Inner Cavity, where pixel and microstrip silicon detectors as well as Transition Radiation detectors are present. Three layers of muon chambers are embedded in the toroidal field generated by one barrel and two End Cap superconducting air-core toroids. However for the present work, only the first muon station (see Fig. 6) is considered, since the layout of the experimental hall as well as of quadrupole shielding etc is dominating the background for the other stations. Schematically the ATLAS detector is supposed to be composed by:

- Inner detector, with Silicon and TRD layers.
- Electromagnetic calorimetry: Lead-liquid argon Barrel and End Cap calorimeters, covering the pseudorapidity range $|\eta| \leq 3.2$
- Hadronic calorimetry: Tile calorimeters (iron-scintillator) in Barrel and Extended Barrel and Copper-liquid Argon in the End Cap, again covering the pseudorapidity range $|\eta| \leq 3.2$
- Forward calorimetry: it is integrated in the same cryostat of the End Cap calorimeters and it is divided in three longitudinal sectors, the first made of Liquid Argon and Copper, the others made of LAr and Tungsten. The pseudorapidity range is $3.2 \leq |\eta| \leq 4.8$.
- Muon chamber system: three superlayers of muon chambers both in the barrel and in the forward region.
- Magnetic field devices: a solenoid in front of the EM barrel calorimeter for the inner tracking, with a Fe return joke outside the hadronic barrel calorimeter. The muon analysing magnetic field is given by one barrel and two forward superconducting air-core toroids.

All the simulated dimensions are as close as possible to reality. Homogenous materials have been used for the calorimeters, keeping the right proportion of constituents.

More details about the detector layout and the simulations carried out for the ATLAS case can be found in [27] and in [28].

5.2 Details of the Simulations

All the calculations have been performed with the code FLUKA. Details about the code and its physical models, as well as benchmarks for both electromagnetic and hadronic applications can be found in [29, 30, 31, 32, 33, 34, 35, 36, 37, 38].

The events used as a source in FLUKA have been generated using PHOJET for all $e^+ - e^-$ calculations, and the code DTUJET93 [39] for the LHC ones.

A major problem in these calculations is the huge amount of CPU time needed to follow all secondaries of a ≈ TeV event down to near-zero energy in a geometry composed by hundreds of different regions. FLUKA, however, allows to use a variety of variance reduction techniques to increase the speed maintaining a good statistics. Different ways of biasing and weighting depending on particle type, position and energy lead to dramatic reduction of CPU time, at the price of losing correlations among different physical quantities, but exactly preserving the average values of any scored quantity. As a result, the CPU time needed for each simulation to reach a satisfactory statistics is of the order of 24 hours on a typical workstation.

Particle transport thresholds have been kept at low values to allow a detailed description of the radiation environment: 30 keV for photons, 0.5 MeV for electrons, 1 MeV for charged hadrons and muons, while neutrons are followed down to thermal energies.

A schematic magnetic field is included in the calculations. A perfect solenoidal 2 T field is assumed in the central cavity, while the Barrel Toroid field has been represented by an azimuthally symmetric toroidal field, with a radial behaviour and a peak value (≈ 1 T) consistent with the ϕ-averaged field of the actual toroid: rough fringe fields have been included.

5.3 Simulated Options

The linear collider project primarily considered in this work is TESLA. Therefore the beamstrahlung parameters used throughout the paper for all calculations are those of TESLA, and when calculations labelled "NLC" are shown, it must be remembered that the same beamstrahlung parameters as for TESLA have been used. However, concerning with integrated average radiation level, that one is the only dependence on the specific project under consideration, once the energy is the same and levels are properly rescaled to a possible different luminosity.

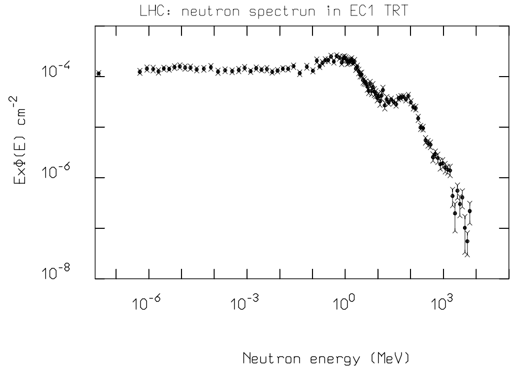

Figure 7: Neutron spectrum for LHC per p–p event, in the TRT detector.

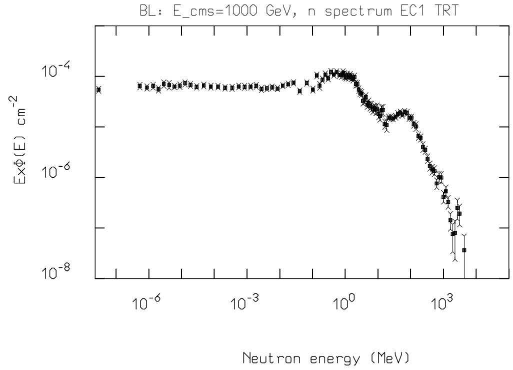

Figure 8: Neutron spectrum at $\sqrt{s} = 1000$ GeV per weighted backscattered laser event, in the TRT detector.

Calculations have been carried out for $\sqrt{s} = 500$ and 1000 GeV, both for the e^+e^- collision option and for the photon–photon one. In the former case, W.–W. and beamstrahlung photon-photon hadronic collisions have been considered and summed together according to the weight given in table 1. In the latter case also the backscattered laser contribution has been added according again to the weight given in Table 1. It must be stressed that since the backscattered laser contribution is largely dominating the other two sources, pos-

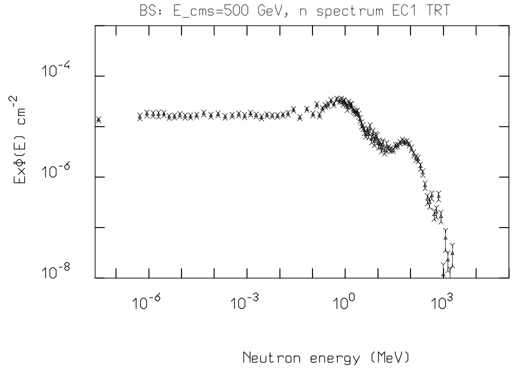

Figure 9: Neutron spectrum at $\sqrt{s} = 500$ GeV per weighted beamstrahlung event, in the TRT detector.

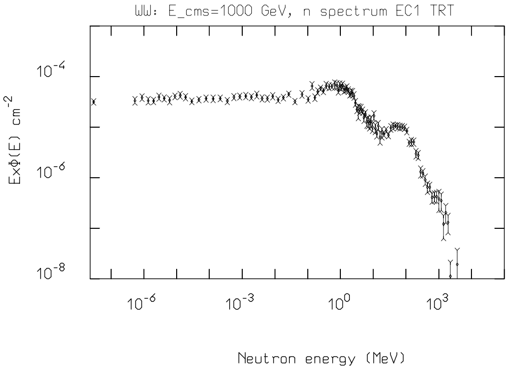

Figure 10: Neutron spectrum at $\sqrt{s} = 1000$ GeV per weighted W.–W. event, in the TRT detector.

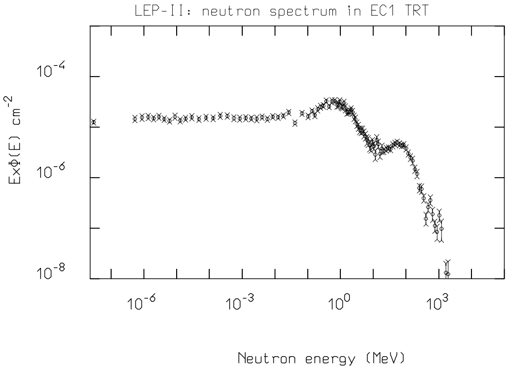

Figure 11: Neutron spectrum for LEP-II per weighted W.–W. event, in the TRT detector.

sible differences in beamstrahlung parameters unless very large, do not show up when comparing different project for the photon collider option.

The parameters used for the calculations are presented in Table 2, together with the corresponding ones for LEP-II and LHC. The integrated luminosity has been obtained from the peak one, just multiplying by 10^7 s, which is the standard year used for all radiation calculations for LHC. A few comments are worthwhile: the figures used for NLC and TESLA may not be the most updated ones, however as far as peak or average luminosities are concerned, a plain scaling can be applied to the presented integrated or peak radiation levels to update them to different values.

The situation is very different when one is looking at peak rates. Indeed sharp differences among different collider designs and hence in the beam time structure, do translate into different scenarios for the instantaneous radiation environment that the various subdetectors will have to stand. One of the most striking differences among a circular machine like LHC where bunches are crossing every 25 ns and the new e^+e^- linear colliders is just in the beam time structure. For all subdetectors but for very fast ones, the LHC beam and hence the related radiation environment is for all practical purposes a continuos beam. Both the drifting/integration time of the various subdetectors and time spread of the soft component of the radiation background contribute to validate such a statement. As an example, two of the ATLAS subdetectors mostly exposed to occupancy problems, the straws of the TRT system and the pressurized drift tubes of the muon chambers, have drifting time in the order of 40 and 300 ns respectively. Therefore the amount of radiation which is of interest for these active elements is the time integral over these periods. Taking into account the interbunch spacing, the time spread of low energy neutrons and photons, and the relatively large number of p–p collisions per bunch crossing the average LHC interaction rate is a fairly good description of the real situation. For most applications the "effective" integrated luminosity experienced by a given active element of integration/drifting time $\Delta Tdet$ is given by:

$$\mathrm{L}_{det-LHC} = L_{LHC} \cdot \Delta_{det} \tag{17}$$

The situation is significantly different for a machine like TESLA where single bunches are separated by a time interval ($\approx 1\mu s$) which is longer than the integration/drifting time of most active elements. To any practical purpose, the peak value of interest is the one connected with a single bunch crossing. An "effective" integrated luminosity can be defined just taking into account the integrated luminosity of each bunch crossing.

$$\mathrm{L}^{eff}_{TESLA} = \frac{L_{TESLA}}{f_{rep} \cdot n_{bunch}} \tag{18}$$

where L_{TESLA} is the average TESLA luminosity, f_{rep} the repetition rate, n_{bunch} the number of bunches per train, and Δt_{det} the integration/drifting time of the active element under consideration. Using the numerical values reported in Table 2 and $\Delta t_{det} \approx 300$ ns which is typical for ATLAS muon chambers, one obtains:

$$\begin{aligned} \frac{\mathrm{L}^{eff}_{TESLA}}{\mathrm{L}^{eff}_{LHC}} &= \frac{L_{TESLA}}{L_{LHC}} \frac{1}{\Delta t_{det} \cdot f_{rep} \cdot n_{bunch}} \\ &= 417 \cdot \frac{L_{TESLA}}{L_{LHC}} \end{aligned} \tag{19}$$

It is rather clear from the above expression that the different time structure of the TESLA beam makes the effective luminosity for "instantaneous" effects much larger than the nominal luminosity, partially compensating the much smaller cross section of photon–photon hadronic interaction with respect to p–p ones. The reason of this effect can be obviously traced back to the much more tightly packed in time luminosity of TESLA, where all the interactions are concentrated in 800 bunch crossings occuring ten times per second instead of being almost uniformly distributed every 25 ns.

But let's now turn our attention to the NLC case. The time structure of NLC is typical of room temperature linear colliders and therefore can be representative of other designs like for example SBLC. Following the previous discussion about L_{eff} a somewhat schematic but good expression for the NLC situation is given by:

$$\begin{aligned} \mathrm{L}^{eff}_{NLC} &= \frac{L_{NLC}}{f_{rep}}, & (20)\\ \Delta T_{det} &> \Delta t_{train} \\ \mathrm{L}^{eff}_{NLC} &= \frac{L_{NLC}}{f_{rep}} \cdot \frac{\Delta t_{det}}{Deltat_{train}}, & (21)\\ \Delta T_{det} &\leq \Delta t_{train} \end{aligned}$$

where $\Delta t_{train} = 126$ ns is the time length of a bunch train. Again using the numerical values of Table 2 one obtains:

$$\begin{aligned} \frac{\mathrm{L}^{eff}_{NLC}}{\mathrm{L}^{eff}_{LHC}} &= \frac{L_{NLC}}{L_{LHC}} \frac{1}{\Delta t_{det} \cdot f_{rep}} = \frac{5.56 \cdot 10^6}{\Delta t_{det}\ [ns]} \frac{L_{TESLA}}{L_{LHC}}, \\ \Delta T_{det} &> \Delta t_{train} = 126\ ns & (22)\\ \frac{\mathrm{L}^{eff}_{NLC}}{\mathrm{L}^{eff}_{LHC}} &= \frac{L_{NLC}}{L_{LHC}} \frac{1}{\Delta t_{train} \cdot f_{rep}} = 4.41 \cdot 10^4 \frac{L_{TESLA}}{L_{LHC}}, \\ \Delta T_{det} &\leq \Delta t_{train} = 126\ ns & (23) \end{aligned}$$

and for in particular for $\Delta t_{det} \approx 300$ ns

$$\frac{\mathrm{L}^{eff}_{NLC}}{\mathrm{L}^{eff}_{LHC}} = 1.85 \cdot 10^4 \frac{L_{TESLA}}{L_{LHC}} \qquad (24)$$

It is apparent from eq. 24 that the "effective" instantaneous luminosity of NLC is much larger than the TESLA one with amplification factors with respect to the nominal average luminosity which range from $\approx 2 \cdot 10^4$ to $4.4 \cdot 10^4$.

Table 2 Parameters used when evaluating the instantaneous and integrated radiation levels for the various linear collider options. Data for LEP–II and LHC are also reported for comparison.

	LEP-II	TESLA	NLC	LHC
$\sqrt{s}$ [GeV]	175	1000 (500)	1000 (500)	14000
L (10^{33})	0.027	5 (2.7)	6 (3.3)	10
$\frac{bunch}{train}$	–	800	90	–
Δt_{bunch} (ns)	–	1000	1.4	25
Rep. rt. (Hz)	–	10	180	–
$\int dtL$ (fb^{-1})	0.27	50 (27)	60 (33)	100

According to Table 1, the ratio between the weights for LHC and the photon collider option at $\sqrt{s}$ = 1000 (500) GeV is $1.3 \cdot 10^5$ ($1.6 \cdot 10^5$), and for the e^+e^- option $2.4 \cdot 10^6$ ($1.8 \cdot 10^6$). The total energy deposited in the detector can be guessed from Table 3 (see next sections) for the various options and it is typically larger for LHC of a factor 3–10 depending on linear collider option and energy. It is already clear at this level that radiation peak values for NLC in the photon collider option can be only a factor 10-100 lower of the (huge) ones anticipated for LHC. It must again be stressed that all numbers presented here take into account only processes like $\gamma\gamma \rightarrow hadrons$ and therefore the overall levels could be even closer to LHC ones.

In the following paragraphs all results for instantaneous levels will be presented using $\Delta t_{det} = 300$ ns just as an example, and the machine parameters presented in Table 2: however the results can be easily rescaled to every different choice using the formulae presented here.

5.4 Results for integrated levels

Before showing maps of the levels, it is important to show how the differences in the physical processes producing hadrons (p–p, W.–W., beamstrahlung and backscattered laser) and in the center of mass energy quickly disappear when particles are showered in the detector. The neutron spectra per (weighted) event calculated in one of the transition radiation assemblies in the detector inner cavity are shown in Fig. 7,8,9, 10,11, for various energies and processes. A part from the absolute normalization which reflects the different average energies and multiplicities among the various processes it is apparent that the same spectrum is generated in all cases.

Maps showing the fluence of neutrons with energies $E_n > 100$ keV, for LHC, TESLA/NLC for the photon collider option and for the e^+e^- one, and for LEP–II for the indicated integrated luminosities and centre of mass energies are shown in Fig. 12,13,14, 15. In these maps as well as in all other maps presented in this work different levels are indicated by a grey scale chosen in such a way to allow to distinguish one level from the following one also in a black and white plot. The grey scale is given in each figure and one specific value is always printed for the point indicated by the arrow, in order to allow a simple matching grey tone–fluence level. The maps for TESLA/NLC are plotted with a scale shifted by seven orders of magnitude with respect to the LHC one. A simple inspection of the maps shows that the contour shapes are similar and that the photon collider option ($\sqrt{s}$ = 500 GeV) is roughly six order of magnitudes lower than LHC, while the e^+e^- one is a further factor ≈20 down. LEP–II levels are plotted with a scale furtherly reduced of five orders of magnitude, and are typically a factor 1000 lower than the corresponding ones of the e^+e^-, $\sqrt{s}$ = 500 GeV, option.

Since the levels appear to be much smaller than LHC ones, the only part of the detector where one could still worry about damage is the central cavity where semiconductor devices are usually installed for tracking. Damage of the silicon detectors can be estimated on the basis of fluences expressed as of 1 MeV neutrons equivalent, using damage functions as given in [40], supplemented with data from [41], for the low-

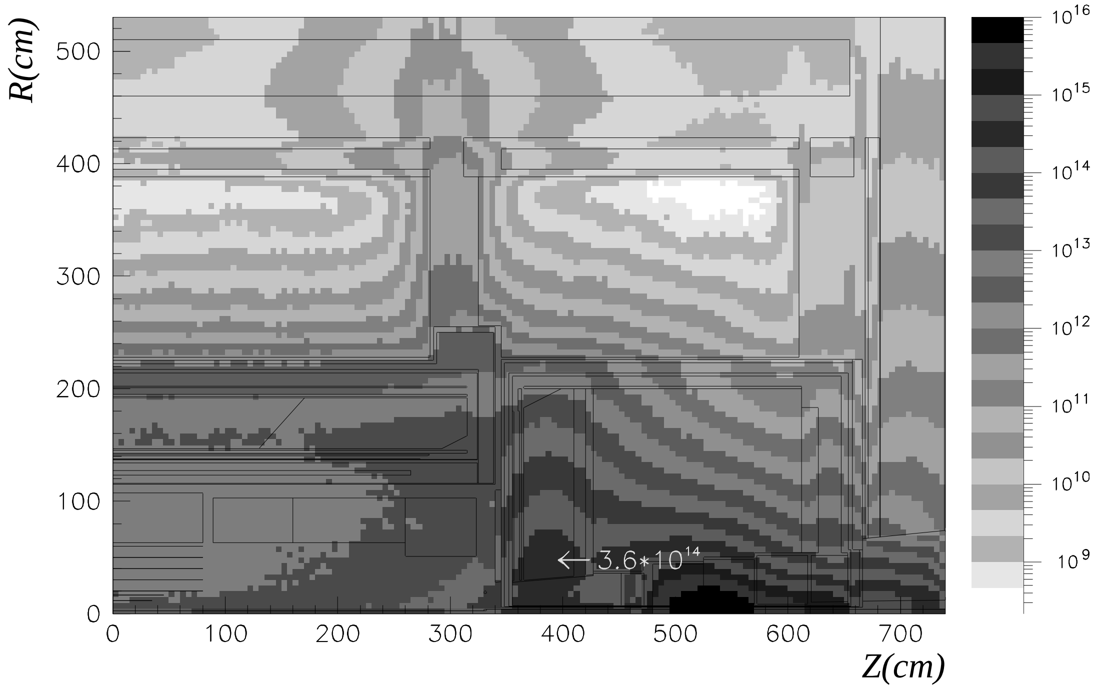

Figure 12: Fluence of neutrons with energy > 100 keV for the LHC case for an integrated luminosity of 100 fb^{-1}.

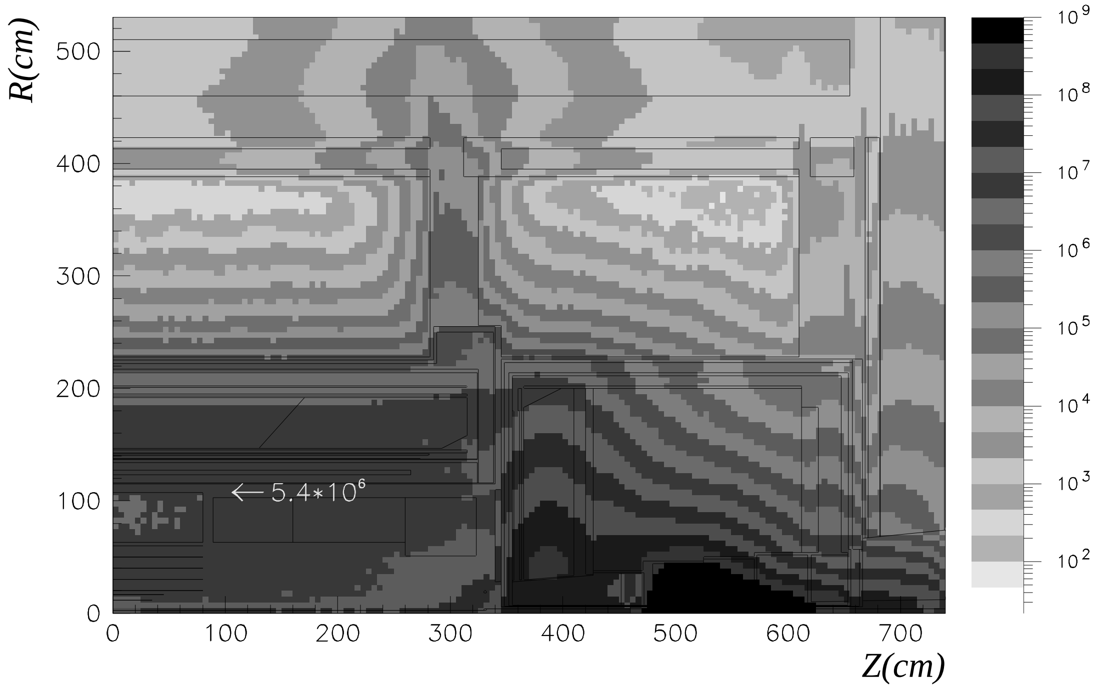

Figure 13: Fluence of neutrons with energy > 100 keV for TESLA/NLC, γ-γ option, for an integrated luminosity of 33 fb^{-1} at $\sqrt{s} = 500$ GeV.

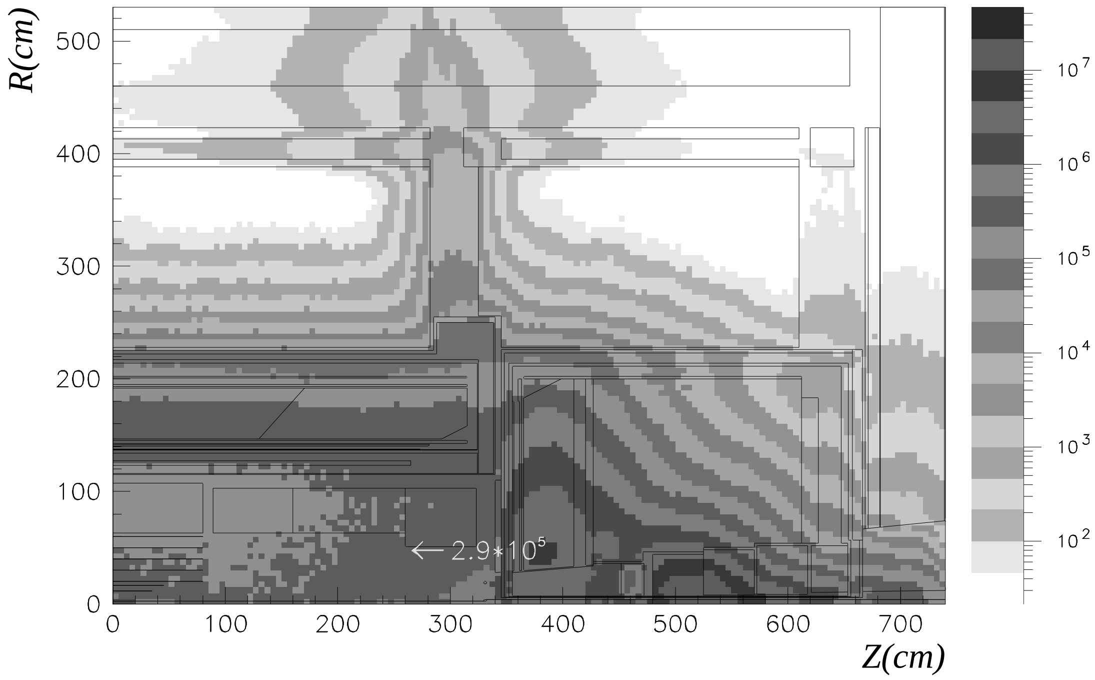

Figure 14: Fluence of neutrons with energy > 100 keV for TESLA/NLC, for an integrated luminosity of 33 fb^{-1} at $\sqrt{s} = 500$ GeV.

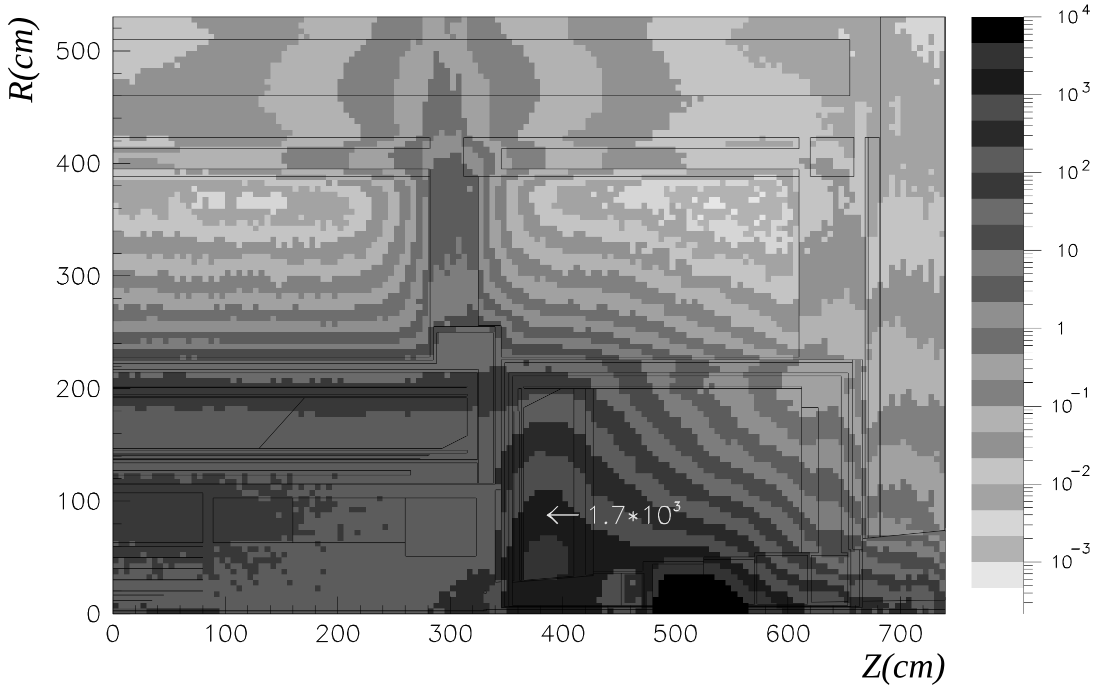

Figure 15: Fluence of neutrons with energy > 100 keV for LEP-II, for an integrated luminosity of 270 pb^{-1} at $\sqrt{s} = 175$ GeV.

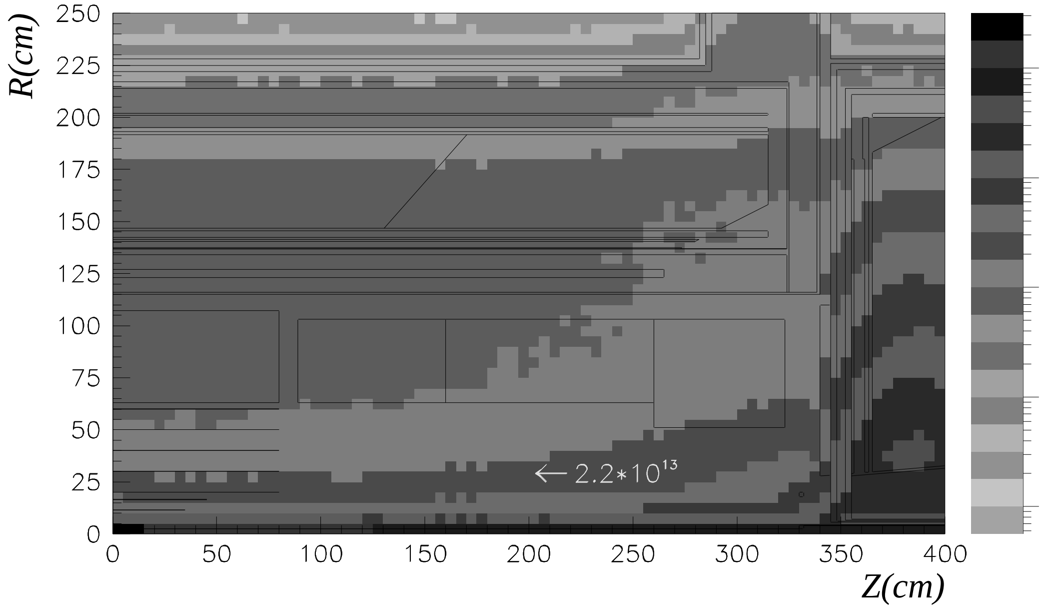

Figure 16: 1 MeV neutron equivalent fluence for LHC, for an integrated luminosity of 100 fb^{-1}.

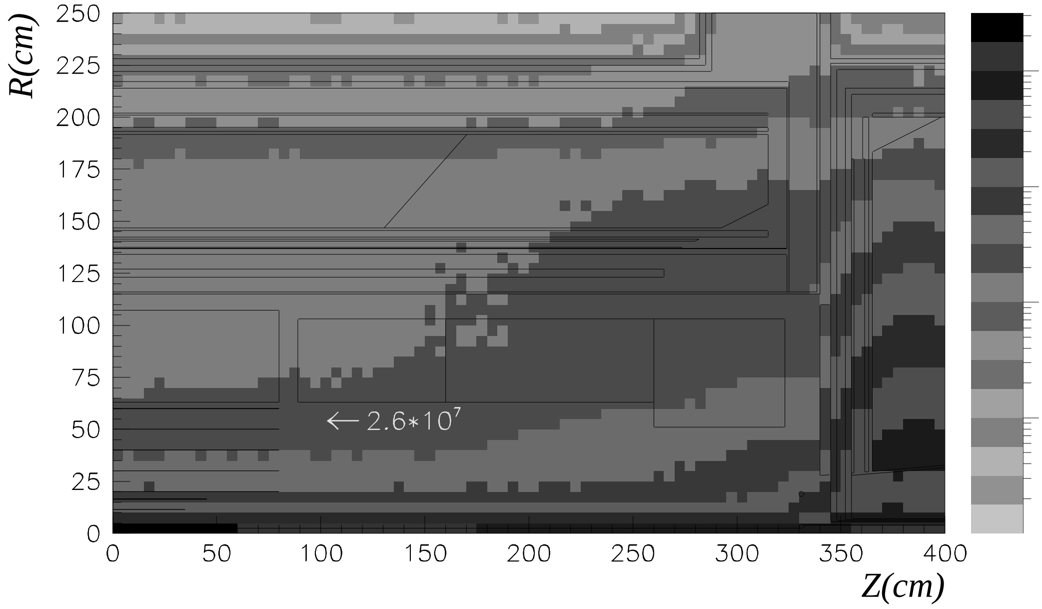

Figure 17: 1 MeV neutron equivalent fluence for TESLA/NLC, for an integrated luminosity of 60 fb^{-1} at $\sqrt{s} = 1000$ GeV due to the backscattered laser source.

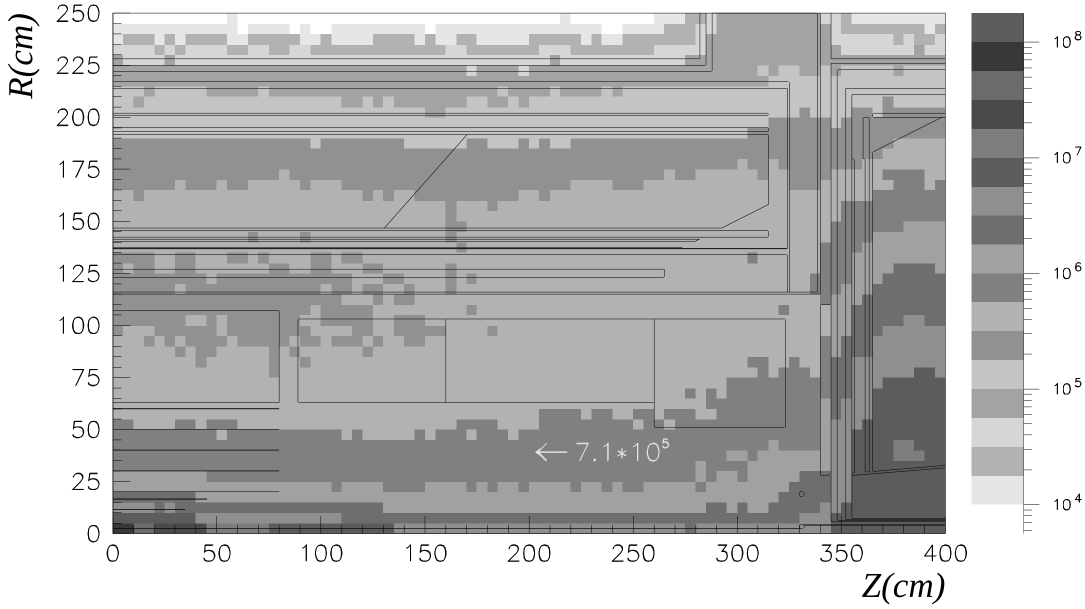

Figure 18: 1 MeV neutron equivalent fluence for TESLA/NLC, for an integrated luminosity of 60 fb^{-1} at $\sqrt{s} = 1000$ GeV due to the beamstrahlung source.

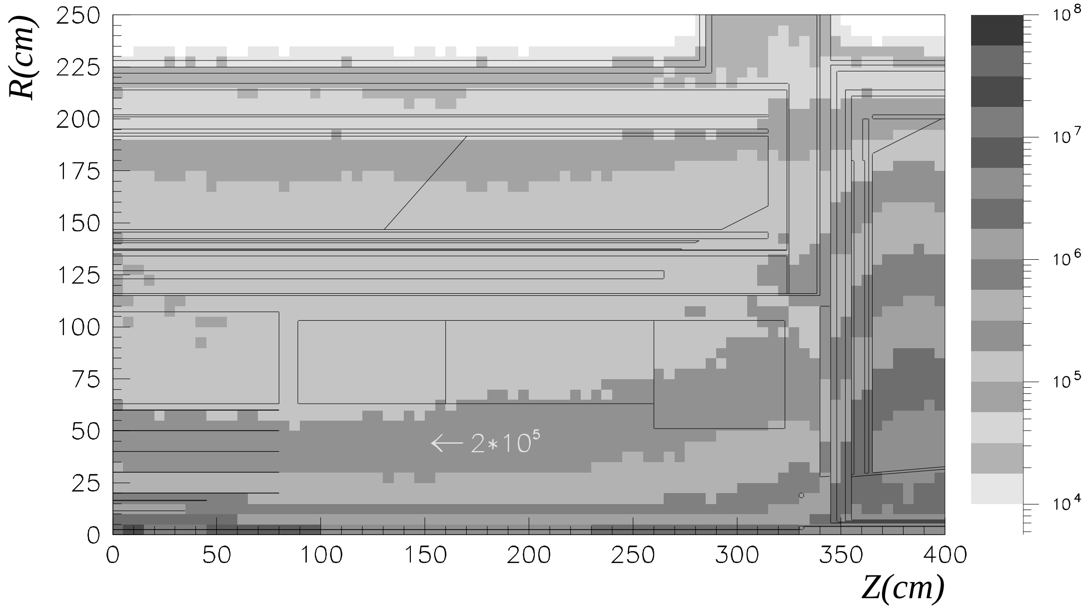

Figure 19: 1 MeV neutron equivalent fluence for TESLA/NLC, for an integrated luminosity of 60 fb^{-1} at $\sqrt{s} = 1000$ GeV due to the W–W source.

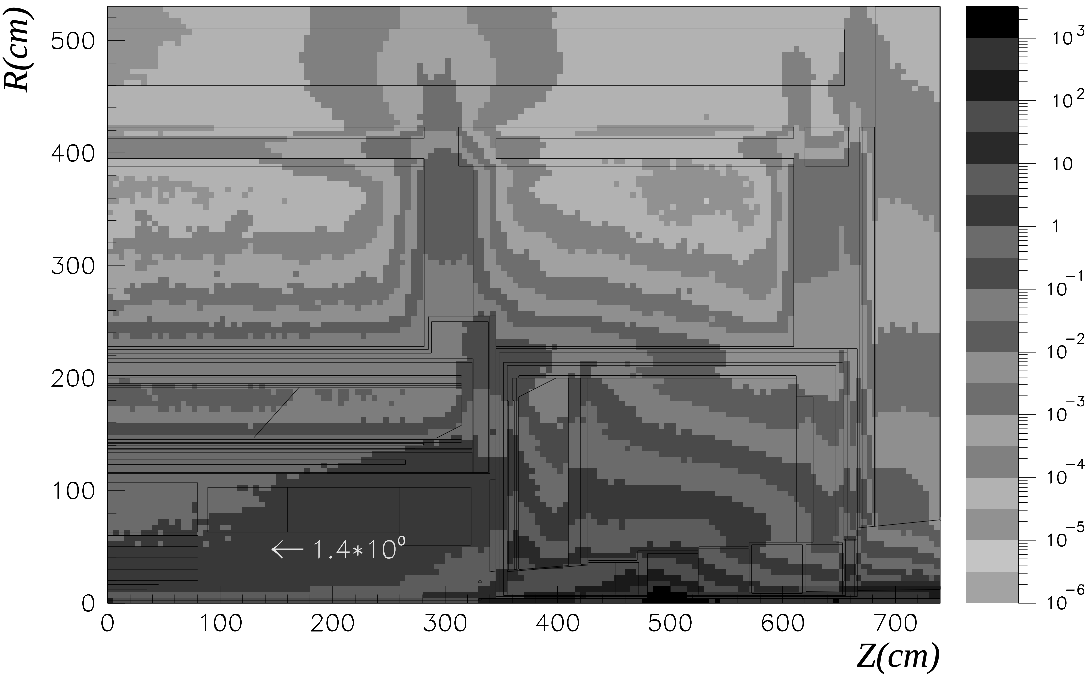

Figure 20: Photon fluence ($E_{ph} > 30$keV) for LHC, integrated over $\Delta t = 300$ ns.

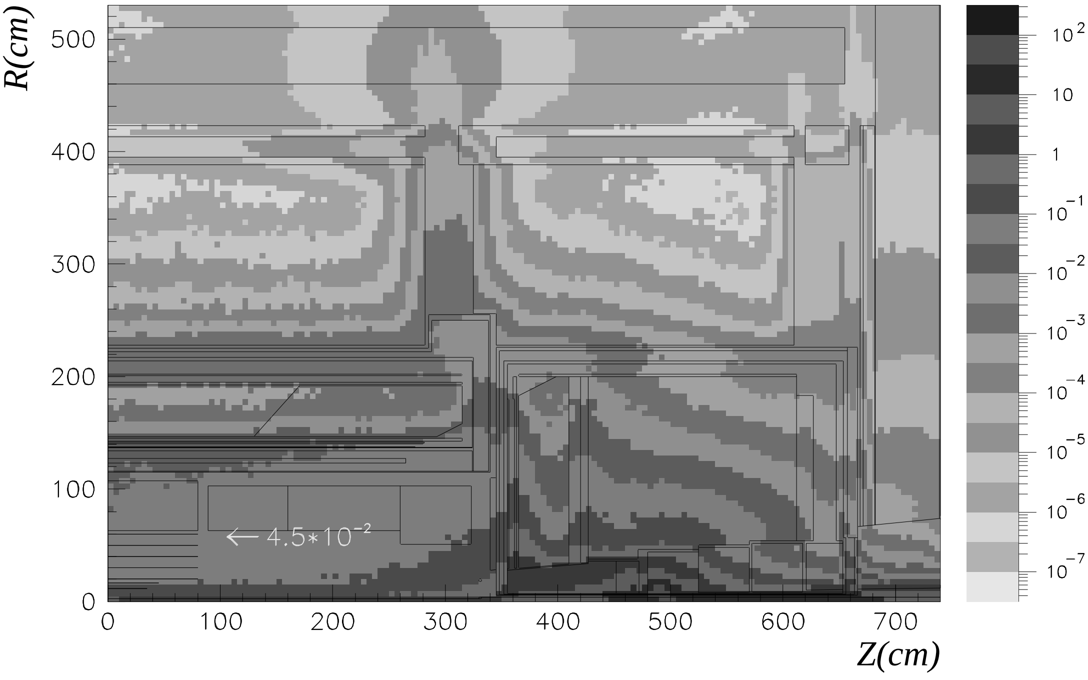

Figure 21: Photon fluence ($E_{ph} > 30$keV) for NLC, integrated over a bunch train $\Delta t = 126$ ns, γ-γ option, at $\sqrt{s} = 1000$ GeV.

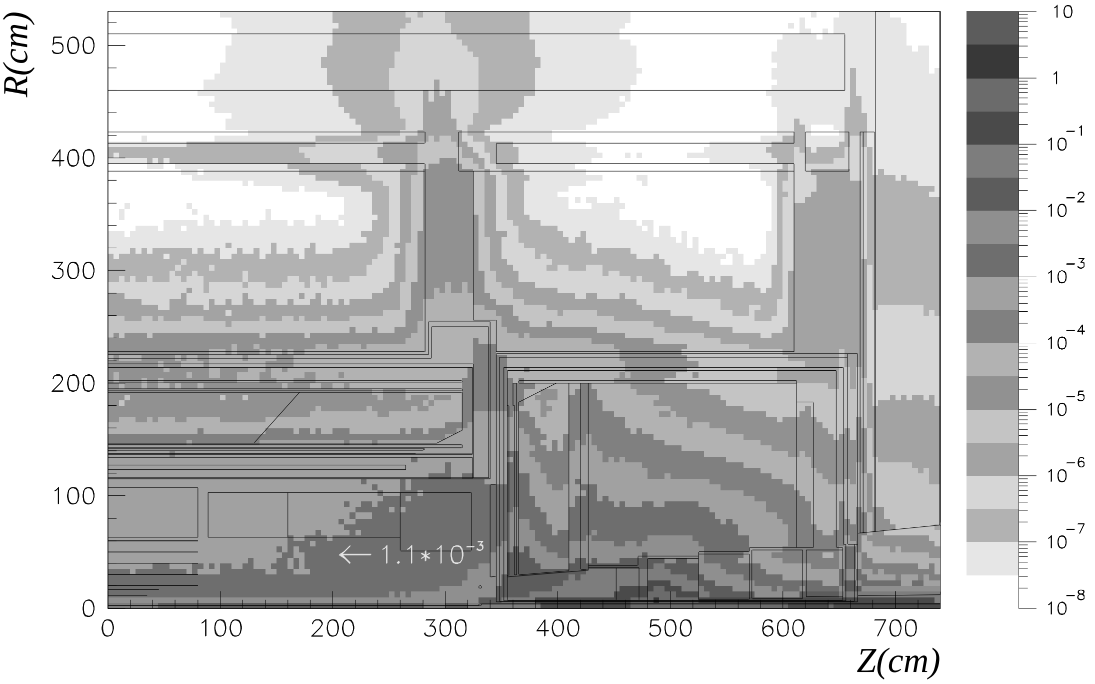

Figure 22: Photon fluence ($E_{ph} > 30$keV) for TESLA for one bunch, γ-γ option, at $\sqrt{s} = 1000$ GeV.

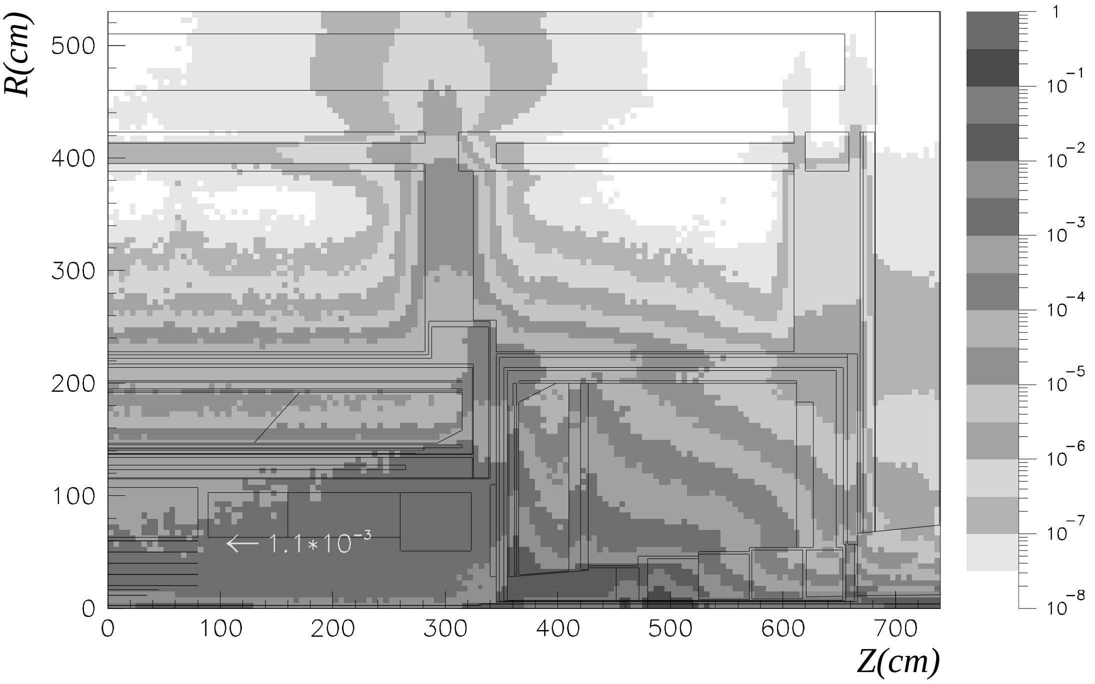

Figure 23: Photon fluence ($E_{ph} > 30$keV) for NLC, integrated over a bunch train $\Delta t = 126$ ns, at $\sqrt{s} = 1000$ GeV.

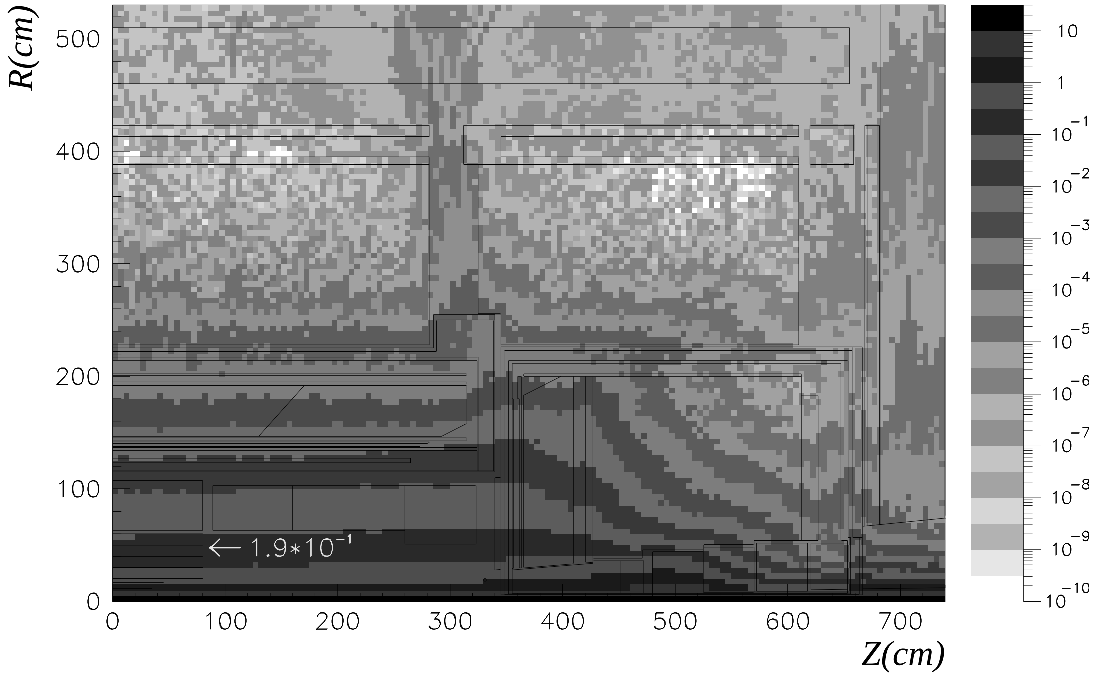

Figure 24: Charged hadron fluence for LHC, integrated over $\Delta t = 300$ ns.

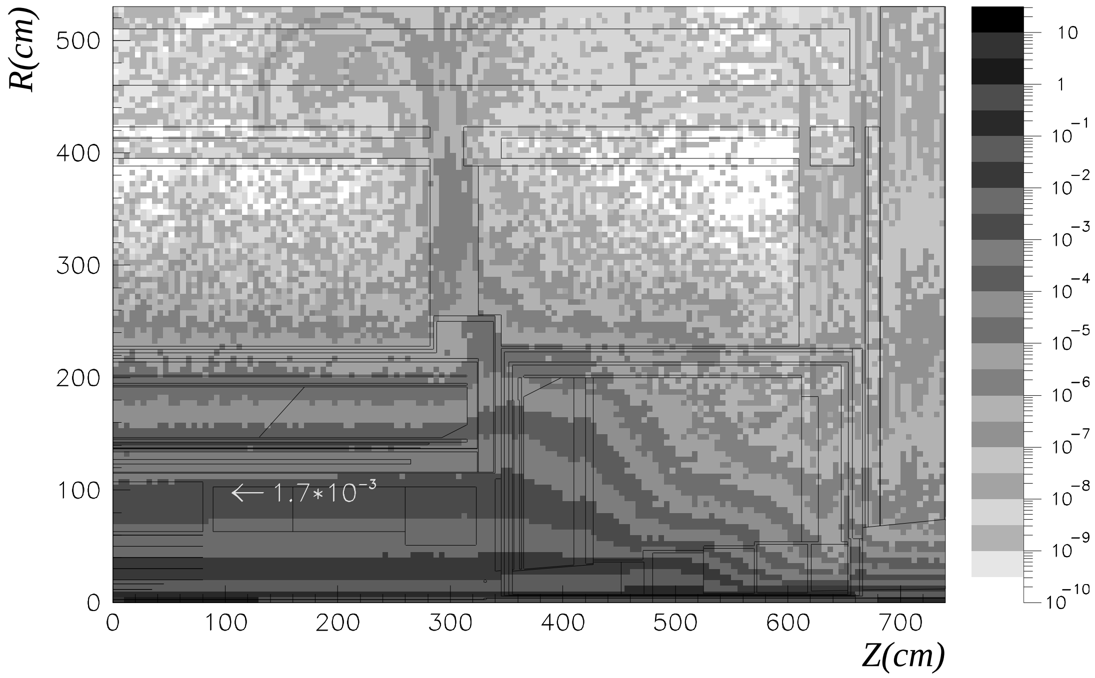

Figure 25: Charged hadron fluence for NLC, integrated over a bunch train $\Delta t = 126$ ns, γ-γ option, at $\sqrt{s} = 1000$ GeV.

est neutron energies. In practice fluences of neutrons and charged hadrons are scored and folded with appropriate damage factors which allow to get a global "1 MeV neutron equivalent fluence" to estimate the damage level. Actually such a fluence will be dominated by charged hadrons coming from the interaction point for the innermost radii, while it will be dominated by low energy neutrons permeating the central cavity at the outermost ones. Maps of the 1 MeV neutron equivalent fluence in the central cavity for LHC, and for backscattered laser, beamstrahlung and W.–W. events at $\sqrt{s} = 1000$ GeV are presented in Fig. 16,17, 18,19 respectively. The maps for the three photon–photon processes are downscaled by a factor 10^6 in the grey scale with respect to the LHC one. It is evident that the backscattered laser source is by far the most intense one, followed by beamstrahlung and W.–W.. The relative importance of silicon damage for the photon collider option (which is the sum of all three processes) and for LHC is typically $5 \cdot 10^{-5}$, with the e^+e^- collider option (dominated by beamstrahlung) further down of a factor ≈ 20.

5.5 Results for instantaneous rates

Let's now turn our attention to instantaneous values. Before going into more details and commenting on fluence maps, it is important to stress a point. The effective integrated luminosities which have been introduced in order to account for the time structure of the beam are actually *average* effective luminosities, where *average* means that event-to-event fluctuations and fluctuations in the number of events per bunch crossing are neglected. These fluctuations are small for LHC, where the average number of p–p collisions per bunch crossing is large ($\approx$20) and several bunch crossings are usually included in the integration/drifting time. For NLC, photon collider option ($\sqrt{s} = 1000$ GeV), the situation is not very different, the average number of "collisions" being $\approx$21 according to the weights of Table 1 and the luminosity of Table 2. For the e^+e^- option, the average number of $\gamma\gamma \rightarrow$ *hadrons* events drops to $\approx$1.1 per bunch train and hence significant straggling in the total amount of particles generated from cycle to cycle can be anticipated. Therefore in this case the *average* effective luminosity and the numbers presented in the following must be taken with care and a proper safety factor of the order 2–3 must be applied to be sure that most of the cycles will produce radiation levels within the quoted range. The same considerations apply to TESLA, photon collider option ($\sqrt{s} = 1000$ GeV), where the average number of photon–photon hadronic collisions per bunch is $\approx$0.5: for the e^+e^- option it drops to $\approx$0.025 and therefore most bunch crossing will be relatively free of hadronic interactions (with a bit of care because of the cut–off used in PHOJET when producing interactions etc) and our effective luminosity has no longer an obvious physical interpretation, there is either no or at least one interaction per bunch crossing.

Maps showing the instantaneous (the one produced by L^{eff}) fluence of photons with energy $E_\gamma >$30 keV for LHC, NLC photon collider and e^+e^- options ($\sqrt{s} =$ 1000 GeV) and for TESLA photon collider version ($\sqrt{s} = 1000$ GeV) are shown in Fig. 20,21, 22,23. Remember that all numbers refer to $\gamma\gamma \rightarrow$ *hadrons* therefore photons generated by other processes are not included in these maps.

Table 3 Average energy deposited in the detector components (E_D) or leaking through the detctori (E_l) (mainly through the forward inner bore) at $\sqrt{s} = 500$ and 1000 GeV, for the three processes under consideration. Both numbers do not include neutrino energy and the energy spent for nuclear binding. Data for LEP–II and LHC are also reported for comparison.

$\sqrt{s}$(GeV)	Photon spect.	E_D (GeV)	E_l (GeV)
175	W.–W.	26	0.8
500	W.–W.	49	10
500	Beamst.	14	0.04
500	B.Laser	196	80
1000	W.–W.	105	43
1000	Beamst.	45	3.2
1000	B.Laser	280	240
$\sqrt{s}$	Hadron spect.		
14000	p-p	850	13100

Contrary to the previous paragraph this time all maps are plotted with the same grey scale, therefore allowing a direct comparison and indicating how effective is the beam time structure in boosting linear collider instantaneous radiation levels when compared with LHC. Levels for NLC, photon collider option, are a factor 30 only below the huge LHC ones. Taking into account that there are important processes like $\gamma\gamma \rightarrow \mu^+\mu^-$ and $\gamma\gamma \rightarrow e^+e^-$ which are not included and that, on the contrary of silicon damage and radioactivation, electromagnetic particles are very effective for detector occupancy, fake tracks etc, these levels are very serious ones and would seriously constrain the design of every detector for such a machine. Just as a matter of example, expected radiation levels for SSC were about one order of magnitude less than for LHC and therefore, once all processes are accounted for, an hypothetical detector sitting at the interactoin point of a room temperature linear collider of the next generation operated will experience a peak radiation field quite comparable to the one anticipated for the SSC experiments. TESLA operated as a photon collider, has a much lower peak value (typically a factor ≈30 lower), thanks to the much more favourable beam time structure. Turning to NLC used as a e^+e^- collider, it can be seen from the maps that photons are still a bit more intense than for TESLA operated as a photon collider, despite the much larger cross section and average centre of mass energy of backscattered laser interactions. For this option, the photon field is typically ≈500 times smaller than for LHC. This is a large number but not a completely comfortable one taking into account the processes not considered, the fluctuations from cycle to cycle discussed above, and the strong constraints and limitations put on LHC detectors by the radiation field that one would surely make much looser for a precision experiment at a linear collider.

As our last example, maps showing the instantaneous fluence of charged hadrons for LHC and NLC photon collider option ($\sqrt{s} = 1000$ GeV) are presented in Fig. 24,25. Considerations similar to those one discussed for photons can be applied also in this case. It can be interesting to remark that the reader can easily convert any of the presented map from integrated to instantaneous levels or viceversa, or from NLC to TESLA for the same energy and option, simply undoing the normalization explained in these paragraphs and making new ones. In this way, the set of maps presented in this work practically covers neutrons above 100 keV, 1 MeV neutron equivalent, photons and charged hadrons, for most of the possible combinations of processes and energies.

In all results presented up to now the effects of radiation components but those interacting in the detector have not been considered at all. However a certain fraction of the particles generated in hadronic photon–photon interactions will escape through the beam pipe or the inner bore of the forward calorimeters, possibly interacting downstream in the experimental hall in some components or in ad hoc shields to protect the final focus quadrupoles. This component is known to be very large at LHC where most of the energy coming from p–p collisions is escaping the detector and creates a huge background of radiation in the experimental hall when interacting with the quadrupole shield (see [27, 42]). No attempt has been made in this work to evaluate the contribution of this component to the stray radiation field in the experimental hall since it is completely dependent on the hall layout, on the presence of shields to protect the final focus quadrupoles and above all on the amount of additional shielding foreseen around all points where interactions will occur in the hall itself. If the contribution coming from sources other than particles interacting in the detector must be kept negligible, such additional shielding can be very substantial. A rough estimate of the importance of this extra source of stray radiation can be derived just looking at the fraction of energy intercepted by the detector itself or streaming through the inner bore for the processes under consideration and reported in Table 3. It is clear that a significant fraction of the energy carried by particles produced in hadronic photon–photon interactions is escaping into the hall. Therefore shielding will be required to protect detectors components like the muon system which would otherwise see the background induced by the interactions of these particles.

6 CONCLUSIONS

Hadronic interactions of quasireal photons occur with cross sections approximately 10 000 times smaller than hadronic interactions of hadrons. The structure of the multihadron events is however remarkably similar to normal inelastic hadronic events. The only striking differences appear in the transverse momentum distribution. The reasons for this are the direct interaction of the photons and the fact, that the photon structure functions are considerably harder than hadron structure functions. PHOJET [4, 5] is the hadronic event generator used in the present study of radiation problems at future Electron–Positron colliders.

The preliminary study presented here clearly demonstrates how e^+e^- linear colliders of the next generation will not provide at all such a clean and well controlled environment that experimentalists hope.

The average integrated hadronic radiation levels at linear colliders might be a factor 10 000 up against the ones expected at LEP–II, however they are about six orders of magnitude below the ones expected at the LHC.

While integrated radiation levels are expected to be well below the levels considered critical for state-of-the-art technologies like those developed for the SSC and LHC detectors, problems connected with radiation induced backgrounds to the experiments can be severe, at least for a few of the accelerator designs. Accelerators operated as photon colliders will experience much higher radiation levels than the ones used in Electro–Positron mode only, and room temperature colliders appear to be much more prone to severe radiation problems than superconducting ones, because of the very different beam time structure.

7 ACKNOWLEDGMENTS

Two of the authors (R.E. and J.R.) are grateful to P. Aurenche for many helpful discussions and suggestions and they acknowledge the hospitality by LAPP, Annecy-le-Vieux. One of the authors (R.E.) was supported by the Deutsche Forschungsgemeinschaft under contract No. Schi 422/1-2.

8 REFERENCES

[1] A. Capella, U. Sukhatme, C. I. Tan and J. Tran Thanh Van: Phys. Rep. 236 (1994) 227

[2] G. A. Schuler and T. Sjöstrand: Nucl. Phys. B B407 (1993) 539

[3] G. A. Schuler and T. Sjöstrand: CERN–TH.7193/94, presented at the Workshop on Two–Photon Physics, Paris, (1994)

[4] R. Engel: Z. Phys. C C66 (1995) 203

[5] R. Engel and J. Ranft: Hadronic photon–photon collisions at high energies, ENSLAPP–A540/95 (hep–ph/9509373), 1995

[6] R. Engel: Multiparticle Photoproduction within the two-component Dual Parton Model, in preparation, 1995

[7] P. Aurenche, F. W. Bopp, A. Capella, J. Kwiecinski, M. Maire, J. Ranft and J. Tran Thanh Van: Phys. Rev. D45 (1992) 92

[8] P. Aurenche, F. W. Bopp, R. Engel, D. Pertermann, J. Ranft and S. Roesler: Comp. Phys. Commun. 83 (1994) 107

[9] M. Glück, E. Reya and A. Vogt: Phys. Rev. D45 (1992) 3986

[10] M. Glück, E. Reya and A. Vogt: Phys. Rev. D46 (1992) 1973

[11] G. A. Schuler: Low- and high-mass components of the photon distribution functions, CERN-TH/95-62, 1994

[12] V. A. Abramovski, V. N. Gribov and O. V. Kancheli: Yad. Fis. C 18 (1973) 595

[13] K. A. Ter-Martirosyan: Phys. Lett. B44 (1973) 377

[14] K. Hahn and J. Ranft: Phys. Rev. D41 (1990) 1463

[15] A. Capella, U. Sukhatme, C. I. Tan and J. Tran Thanh Van: Z. Phys. C C10 (1980) 249

[16] A. B. Kaidalov: Phys. Lett. B116 (1982) 459

[17] H. U. Bengtsson and T. Sjöstrand: Comp. Phys. Commun. 46 (1987) 43

[18] C. F. von Weizsäcker: Z. Phys. 88 (1934) 612

[19] E. J. Williams: Phys. Rev. 45 (1934) 729

[20] S. Frixione, M. Mangano, P. Nanson and G. Ridolfi: Phys. Lett. B319 (1993) 339

[21] P. Chen, T. L. Barklow and M. E. Peskin: Phys. Rev. D49 (1994) 3209

[22] M. Drees and R. M. Godbole: Z. Phys. C C59 (1993) 591

[23] I. F. Ginzburg, G. L. Kotkin, V. G. Serbo and V. I. Telnov: Nucl. Instrum. Methods A205 (1983) 47

[24] I. F. Ginzburg, G. L. Kotkin, V. G. Serbo and V. I. Telnov: Nucl. Instrum. Methods A219 (1984) 5

[25] V. I. Telnov: Nucl. Instrum. Methods A294 (1990) 72

[26] R. Brinkmann: SBLC and TESLA general design overview, Presentation at the Linear Collider workshop, Gran Sasso, Italy, 1995

[27] Atlas Collaboration: Technical Proposal of the ATLAS collaboration, CERN/LHCC/94-43, LHCC/P2, 1994

[28] A. Fassò, A. Ferrari, K. Potter and S. Rollet: Radiation calculations for the ATLAS detector and experimental hall, this conference, 1995

[29] A. Ferrari, P. R. Sala, G. Guaraldi and F. Padoani: Nucl. Instr. Meth. **B71** (1992) 412

[30] P.-A. Aarnio et al.: Proc. of the MC93 Int. Conf. on Monte Carlo Simulation in High-Energy and Nuclear Physics, Feb. 22-26, 1993. Ed. P. Dragovitsch, S.L. Linn, M. Burbank, World Scientific, Singaporei, p.89, 1994

[31] P.-A. Aarnio et al.: Proc. of the MC93 Int. Conf. on Monte Carlo Simulation in High-Energy and Nuclear Physics, Feb. 22-26, 1993. Ed. P. Dragovitsch, S.L. Linn, M. Burbank, World Scientific, Singaporei, p.100, 1994

[32] P. R. Sala and A. Ferrari: Proc. of the MC93 Int. Conf. on Monte Carlo Simulation in High-Energy and Nuclear Physics, Feb. 22-26, 1993. Ed. P. Dragovitsch, S.L. Linn, M. Burbank, World Scientific, Singaporei, p.277, 1994

[33] A. Fassò, A. Ferrari, J. Ranft, P. R. Sala, G. R. Stevenson and J. M. Zazula: Nucl. Instr. & Meth. A**332** (1993) 459

[34] A. Fassó et al.: FLUKA92, *Proc. of the workshop on Simulating Accelerator Radiation Environment*, SARE, Santa Fè, 11-15 january (1993), A. Palounek ed., Los Alamos LA-12835-C 1994, (p. 134)., 1994

[35] C. Birattari, E. De Ponti, A. Esposito, A. Ferrari, M. Pelliccioni and M. Silari: Nucl. Instr. & Meth. A**338** (1994) 543

[36] A. Fassò, A. Ferrari, J. Ranft, and P.R. Sala: FLUKA:present status and future developments, *Proc. of the IV Int. Conf. on Calorimetry in High Energy Physics*, La Biodola, September 21-26, 1993, Italy, World Scientific, Singapore (1994) p. 493., 1994

[37] A. Fassò, A. Ferrari, J. Ranft, and P. R. Sala: FLUKA: Performances and Applications in the Intermediate Energy Range, *Proc. of the "Specialists' Meeting on Shielding Aspects of Accelerators, Targets & Irradiation Facilities"*, Arlington, April 28-29 1994, published by OECD/NEA (1995), 287., 1995

[38] A. Fassò, A. Ferrari, J. Ranft, and P. R. Sala: An update about FLUKA, this conference, 1995

[39] F. W. Bopp, R. Engel, D. Pertermann, J. Ranft and S. Roesler: Comp. Phys. Commun. 83 (1994) 107

[40] M. Huhtinen and P.A. Aarnio: NIM A335 (1993) 580

[41] A.M. Ougouag et al.: IEEE Trans. Nucl. Sci. **37** (1990) 2219

[42] CMS Collaboration: Technical Proposal of the CMS collaboration, CERN/LHCC/94-38, LHCC/P1, 1994